

Contents lists available at ScienceDirect

Journal of the Mechanics and Physics of Solids

journal homepage: www.elsevier.com/locate/jmps



Comparing inelastic deformations and strength in dense FCC and HCP granular crystals: Experiments and models



Tian Gao, Ashta Navdeep Karuriya, Francois Barthelat *

Department of Mechanical Engineering, University of Colorado, 427 UCB, 1111 Engineering Dr. Boulder, CO 80309, United States

ARTICLE INFO

Keywords:
Granular crystals
Granular mechanics
Granular metamaterials
Crystal plasticity
Crystallography
FCC (Face-centered cubic)
HCP (Hexagonal close-packed)

ABSTRACT

Randomly distributed granular materials offer a rich landscape of mechanisms but their tunability is limited. Taking inspiration from crystallography and granular mechanics, we fabricated and tested fully dense cohesive FCC and HCP granular crystals, and developed granular crystal plasticity models to investigate their relative strength and deformation mechanisms. Geometrically, switching from FCC to HCP is remarkably simple and only involves a 60° rotation about the midplane of individual dodecahedral grains. However, the effect of this transformation on crystallography, properties and mechanics are profound. This rotation breaks several symmetries, and while additional slip systems are made available (prismatic, pyramidal.) compared to the {111} family in FCC, each of the families in HCP contain a smaller number of total slip planes. As a result, slip in HCP is in general more difficult to activate resulting in an average strength 50% greater than in FCC. We also observed mechanisms that are unique to granular crystals: microbuckling in FCC and HCP, and splaying in HCP crystals loaded along the c-axis. These granular crystals offer powerful and versatile platforms for new generation mechanical metamaterials with tunable inelastic deformation, energy absorption and strength. For example, the granular architecture amplifies the properties of the adhesive by about one order of magnitude, so that attractive rheologies maybe be translated into useful responses in compression.

1. Introduction

Granular materials can be defined as a large collection of discrete, macroscopic particles which interact mainly by frictional contact forces (Jaeger et al., 1996). Granular materials are seemingly simple systems, but they in fact display a wide range of complex nonlinear mechanical responses and behaviors (de Gennes, 1998; Jaeger et al., 1996). Typical granular materials are based on spherical grains, which is sub-optimal in terms of mechanical performance: The random packing of spheres leads to a solid volume fraction of only 0.55 to 0.64 (Onoda and Liniger, 1990), which is significantly smaller than the maximum close packing volume fraction (0.74). In addition, internal forces and stresses in sphere-based granular materials are transmitted from grain to grain over small contact areas, resulting in high, concentrated stresses. Applied mechanical loads are channeled in the material along localized force lines that occupy only a small volume in the material (Behringer et al., 2014) while most grains remain free of stress, and deformation mechanisms are governed by the formation of clusters, localized regions of stress transfer, jamming, and shear bands (Behringer and Chakraborty, 2018; Radjai et al., 2017).

While the strength of granular material may be increased to some extent by tailoring the shape of the individual grains

E-mail address: francois.barthelat@colorado.edu (F. Barthelat).

https://doi.org/10.1016/j.jmps.2025.106305

^{*} Corresponding author.

(Athanassiadis et al., 2014), the inherent randomness of typical granular materials remains a severe limitation to efficient designs that fully exploit deformation mechanisms. Another approach to increasing mechanical performance in granular systems involves the ordered arrangement of grains into periodic constructs - termed granular crystals - through controlled manipulation of particle shape, interfacial interactions, and compaction protocol (AlMahri et al., 2023; Karuriya and Barthelat, 2023; Villarruel et al., 2000). Using Monte Carlo simulations, Glotzer and co-workers demonstrated how the shape of the individual particles that assemble under entropic forces give rise to distinct structures including FCC, BCC, rhombohedral or liquid crystals (Damasceno et al., 2012). On the experimental side, 3D colloidal lattices can be created with 100 nm spheres in solution (Henzie et al., 2012). Interestingly, these colloidal crystals can be also used as model materials to explore and better understand atomic scale deformation mechanisms: 3D dislocation dynamics (Schall et al., 2004), effects of grain boundaries (Maire et al., 2016). At larger scales, topologically interlocked materials can be interpreted as 2D granular crystals which can not only be much tougher (× 50) than monolithic plates of the same material, but also stronger (Mirkhalaf et al., 2018), Millimeter-scale 3D printed grains of specific geometries can be assembled into fully dense FCC and BCC crystals which are 10 times stronger than traditional granular materials (Karuriya and Barthelat, 2023), and which can also be infused with adhesives (Karuriya et al., 2024). These granular crystals display a rich set of mechanisms: Nonlinear deformations, crystal plasticity reminiscent of atomistic mechanisms, geometric strain hardening, shear-induced dilatancy, micro-buckling (Karuriya and Barthelat, 2023). An interesting approach to harvesting these mechanisms is to look at classical metallurgy for inspiration. The effects of defects, grain boundaries and alloving have yet to be translated to granular materials at larger length scales. Another interesting aspect to designing granular crystals is to manipulate crystallography. For example, hexagonal closed packed (HCP) metals such as titanium or magnesium tend to be stronger (higher yield stress) than face centered cubic (FCC) metals such as aluminum and copper (Jiang et al., 2023; Lin et al., 2018; Lu et al., 2023; Niu et al., 2018; Yang et al., 2018). The mechanical difference between HCP and FCC metals lies in their dislocation movement and slip systems, stemming from distinct atomic arrangements. FCC metals, such as aluminum, have 12 slip systems that allow easy dislocation motion. This results in high ductility, but at the expense of strength (Lin et al., 2018; Lu et al., 2023). In contrast, HCP metals typically have only 3-4 slip systems, which restricts dislocation motion and enhances strength (Jiang et al., 2023; Niu et al., 2018; Yang et al., 2018). HCP metals also exhibit elastic anisotropy and twinning mechanisms, greatly increasing strength along specific crystallographic orientations, particularly along the c-axis of the hexagonal unit cell (Antonangeli et al., 2006; Arul Kumar et al., 2016; Meyers et al., 2001). In this report we investigate whether these atomic scale strengthening mechanisms can be duplicated at the macroscale in fully dense FCC and HCP granular crystals. We first discuss the design and fabrication of these crystals and results from compression tests on these crystals. We then present granular crystal plasticity models that are validated with experiments, and which we use for comparative analysis of strength and failure modalities in FCC and HCP crystals.

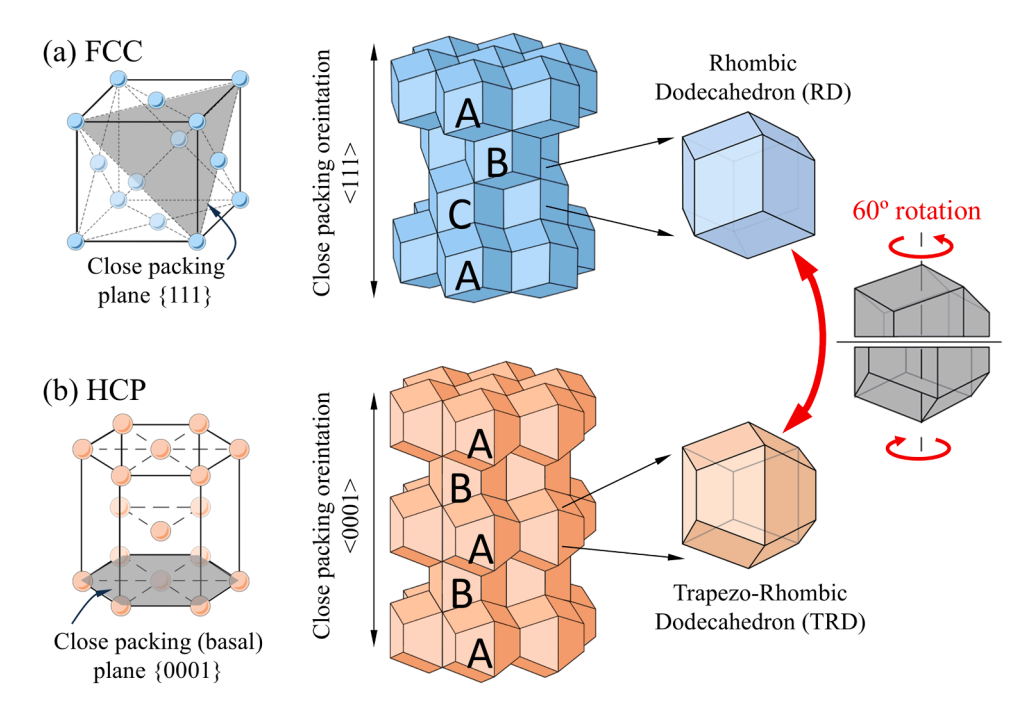


Fig. 1. Close packed granular crystals: Lattice and unit cells, packing sequence and individual grain geometries for (a) Face centered cubic (FCC) and (b) Hexagonal close packed (HCP) crystals. The individual grain for the FCC crystal (Rhombic dodecahedron) can be transformed into the individual grain for the HCP crystal (Trapezo-rhombic dodecahedron) by a 60° rotation about the $\langle 111 \rangle$ FCC direction (c-axis for the HCP crystal).

2. Close packed and fully dense granular crystals

An interesting and useful feature of space filling polyhedra is that they can be found from 3D Voronoi decompositions on predetermined lattices. For example, taking the atomic positions of a face-centered-cubic lattice as seeds for a Voronoi decomposition produces a spatial tessellation of solid rhombic dodecahedra (RD), each composed of twelve identical rhombic faces (Fig. 1a). A representation of this crystalline structure with the {111} direction oriented vertically shows the classical stacking sequence ABCA of the closed packed layers in FCC crystals (Callister and Rethwisch, 2020). The individual unit cells may be interpreted as a Wigner-Seitz cell in crystallography (Kettle and Norrby, 1994), but in our case we use the geometry of the cells to create polyhedral grains millimeters in size. Conversely, a Voronoi decomposition of a hexagonal close-packed (HCP) lattice yields trapezo-rhombic dodecahedra (TRD, Fig. 1b). A representation of this crystalline structure with the [0001] direction (or "c-axis") oriented vertically reveals the classical stacking sequence ABA of the closed packed layers in HCP (Callister and Rethwisch, 2020). FCC and HCP lattices share many traits. In terms of spatial arrangement, they are both close-packed and only differ by their stacking sequence. Their Wigner-Seitz cell, or grain, are both dodecahedra, and interestingly one can shift from one to the other shape by a simple 60° rotation about the $\langle 111 \rangle$ axis of the FCC, or equivalently about the c-axis of the HCP (Fig. 1). Importantly, this rotation breaks many of the symmetries in the rhombic dodecahedron (RD). For example, while all faces of the RD are rhombuses, in TRD six of the faces are rhombuses, while the other six are isosceles trapezoids. This simple rotation not only changes the combinatorial structure and geometry of the unit cells, but it also transforms the highly symmetry group O_h of RD into the low symmetry group D_{3h} of TRD. As discussed above, the lower symmetry of HCP metals generally leads to higher strengths compared to FCC metals. The main hypothesis of this study was that this increase of strength from FCC to HCP could also be translated to macroscale granular crystals.

3. Fabrication

The granular systems we considered contained N = 380 grains each, which occupied an approximate volume of $30 \times 30 \times 100$ mm³, with small variations depending on crystal orientation. We fabricated individual grains using a high-resolution 3D printer based on digital light processing (DLP, EnvisionTEC Micro HiRes, Fig. 2a). This printer produces individual grains which are fully dense, isotropic, and with a smooth surface comparable to injection molding. The grains were made of a photocurable resin which is relatively stiff (measured Young's modulus = 3 GPa) and strong (measured yield strength = 70 MPa). The volume of the grains was exactly 132 mm³ for both TRD and RD grains, corresponding to a size of 5.71 mm (face-to-face distance).

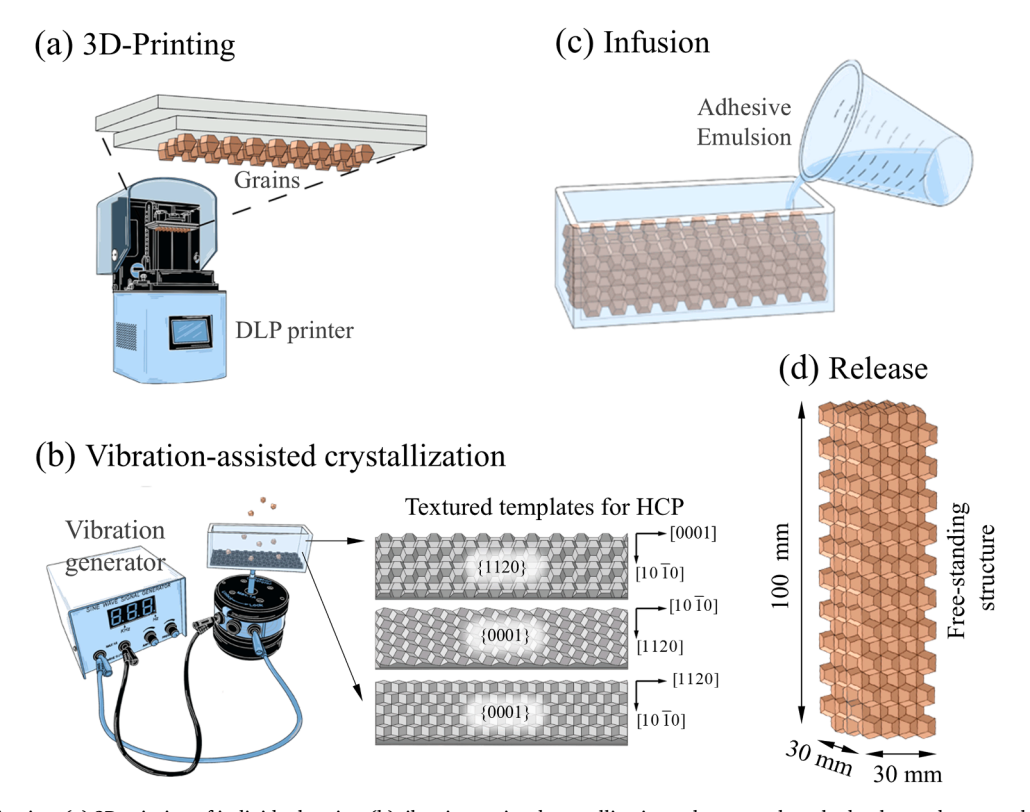


Fig. 2. Fabrication. (a) 3D printing of individual grains; (b)vibration-assisted crystallization, where templates had to be used to assemble the lower-symmetries HCP crystals; (c) Infusion of an emulsion of ethanol and pressure sensitive adhesive. After evaporation of ethanol, the free-standing crystal is (d) released from the assembly box.

We randomly poured 380 of these grains into a $126 \times 33 \times 42$ mm³ assembly box mounted on a vibration generator (Fig. 2b). To assemble the FCC crystals, vertical vibrations with amplitude ~ 2 mm and frequency ~ 18 Hz were applied on the box to induce the assembly of the grains. The assembly of the FCC crystals did not require additional templates other than the box itself: The container floor served as template to crystallize {111} close-packing planes. The densest linear packing orientation $< 1\overline{10} >$ also aligned with the vertical walls, forming near fully dense FCC crystals with either the $< 1\overline{21} >$ orientation or the $< 1\overline{10} >$ orientations aligning with the

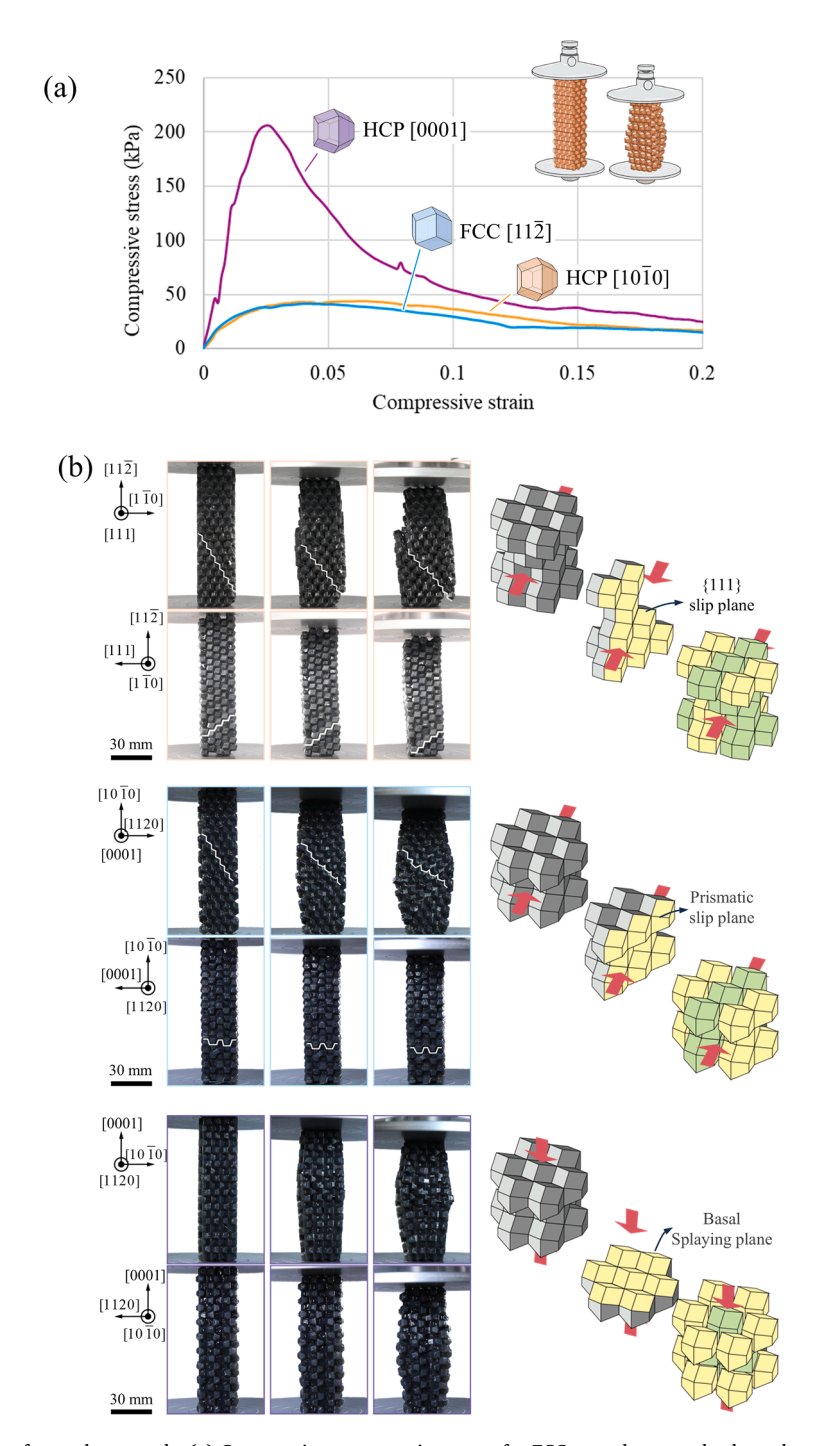


Fig. 3. Ductile responses of granular crystals. (a) Compressive stress-strain curves for FCC granular crystals along the $<1\overline{2}1>$ loading direction (light blue), and HCP granular crystals along the $<10\overline{1}0>$ (orange) and <0001> (purple) loading directions; (b) Snapshots of the samples at different stage of compression show grain-on-grain sliding along slip planes and grain-on-grain splay deformation for the FCC/ $<1\overline{2}1>$ and the HCP $/<10\overline{1}0>$ tests. The HCP /<0001> tests revealed a different type of ductility where the grains collectively slide over large volume and in a splaying fashion.

longer walls of the container (Karuriya et al., 2024; Karuriya and Barthelat, 2023). While the assembly of FCC crystals was relatively easy and fast, assembling HCP crystals from TRD grains using the same protocol was not successful, because of the lower symmetries of TRD grains. While RD grains can rotate to either one of eighteen orientations to align and assemble within the closed-packed {111} plane, in the TRD grains there are only six orientations which enable the assembly of a closed-packed basal plane. To properly initiate the crystallization of TRD grains, we 3D printed templates with different textures, which we inserted on the floor of the container before crystallization.

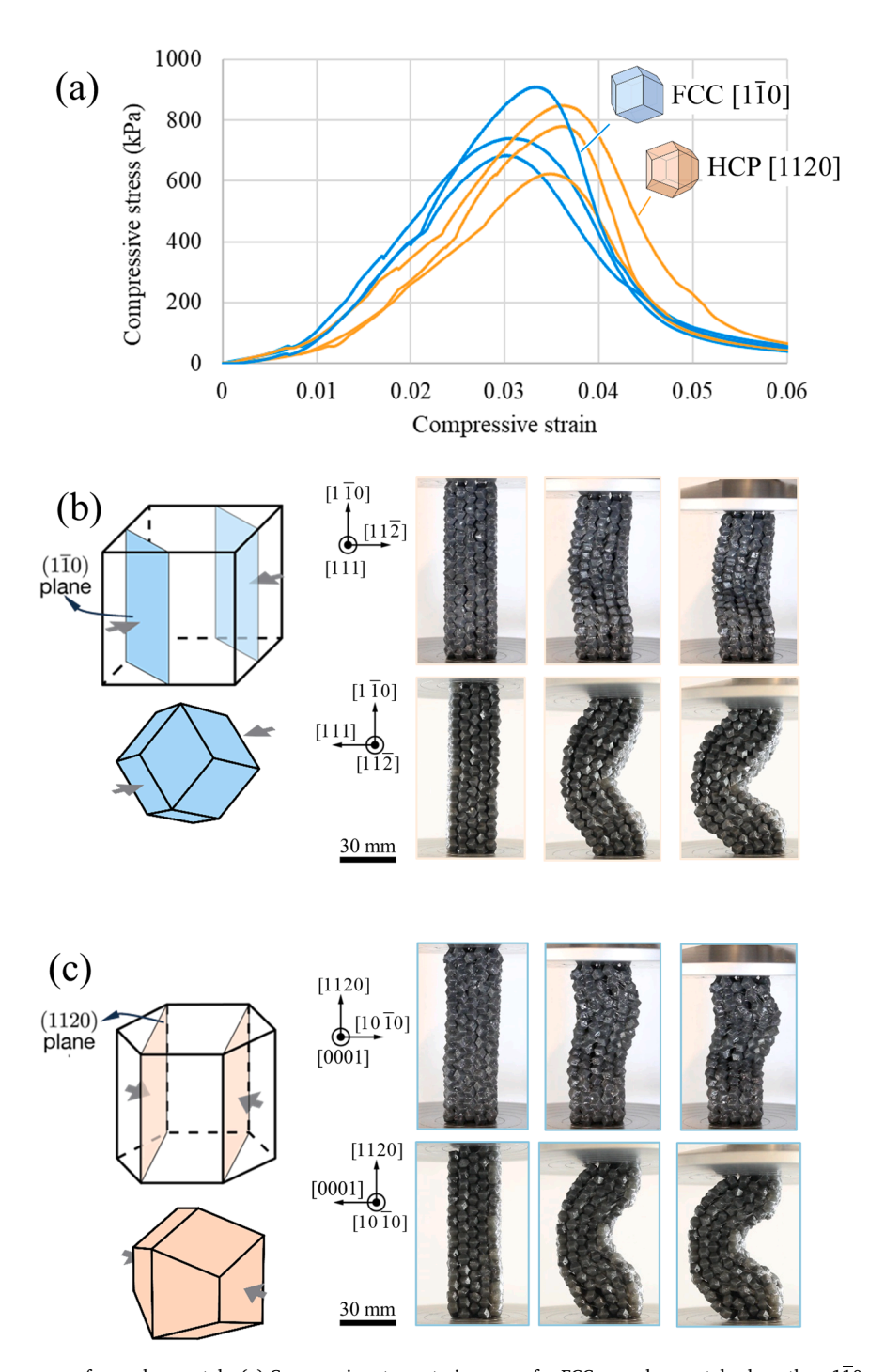


Fig. 4. Buckling responses of granular crystals. (a) Compressive stress-strain curves for FCC granular crystals along the $< 1\overline{10} >$ loading direction (blue), and HCP granular crystals along the $< 11\overline{20} >$ loading direction (orange); Snapshots of the samples at different stage of compression showing collective buckling of (b) FCC and (c) HCP granular crystals.

Fig. 2b shows the three different crystallographic textures we created and used: A $\{11\overline{2}0\}$ template with the $<10\overline{1}0>$ oriented along the long axis of the container, a $\{0001\}$ template with the $<11\overline{2}0>$ oriented along the long axis of the container, and a $\{0001\}$ template with the $<10\overline{1}0>$ oriented along the long axis of the container. In addition, instead of crystallizing a large volume of grains at once, we dropped individual grains in the vibrating assembly box, which enabled a layer-by-layer, epitaxial growth of the HCP crystal (see supplementary movie S1). Once the grains were assembled into granular single crystals, the interfaces were infiltrated by a pressure sensitive adhesive (Aleene's Repositionable Tacky Spray (P.F. Aleene's Repositionable Tacky Spray 10 oz, 2025), Fig. 2c). We first prepared an emulsion of this adhesive and ethanol in the ratio of 2:3, which we poured onto the crystalized grains. This emulsion has low viscosity and no adhesion, so the interfaces between the grain were fully infiltrated. We finally evaporated the ethanol from the crystal, which left a thin layer of adhesive at the interfaces between the grains. The granular crystal was finally extracted from the assembly box as a free-standing structure (Fig. 2d).

The choice of adhesive was critical to achieve large inelastic deformations in the granular crystals: A strong adhesive would make the interfaces between grains mechanically invisible, and grains bonded this way would behave like monolithic polymers. Cohesive interfaces which are weaker than the grains are indeed critical, so deformation and sliding are channeled at the interfaces between the grains (interestingly many hard biological like bone, wood or mollusk shells rely on weak interfaces to generate toughening mechanisms (Barthelat et al., 2016)). The methacrylate-based pressure sensitive adhesive (PSA, Aleene's Repositionable Tacky Spray (P.F. Aleene's Repositionable Tacky Spray 10 oz, 2025)) we selected is relatively weak (strength $\sim 100 \text{ kPa}$) compared to the grains (strength $\sim 70 \text{ MPa}$) and it can sustain adhesion over a very large range of normal and shear strains (Karuriya et al., 2024), enabling large inelastic deformations concentrated at the interfaces between the grains.

4. Compression tests on FCC and HCP crystals

Once fabricated, the close packed granular crystals were tested in uniaxial compression along their long axes, using a standard testing frame (ADMET eXpert 5603) mounted with smooth steel compression plates. We used quasi-static rate of 330 μ m /sec, corresponding to a compressive strain rate of $\sim 3.3 \times 10^{-3} \ s^{-1}$. Pictures of the samples were acquired at regular intervals during the test. True stress and true strain were calculated from the force and displacements using standard procedure, accounting for the large change in specimen length and changes in cross section observed in the experiments. The results (Figs. 3 and 4) show that the strength of the

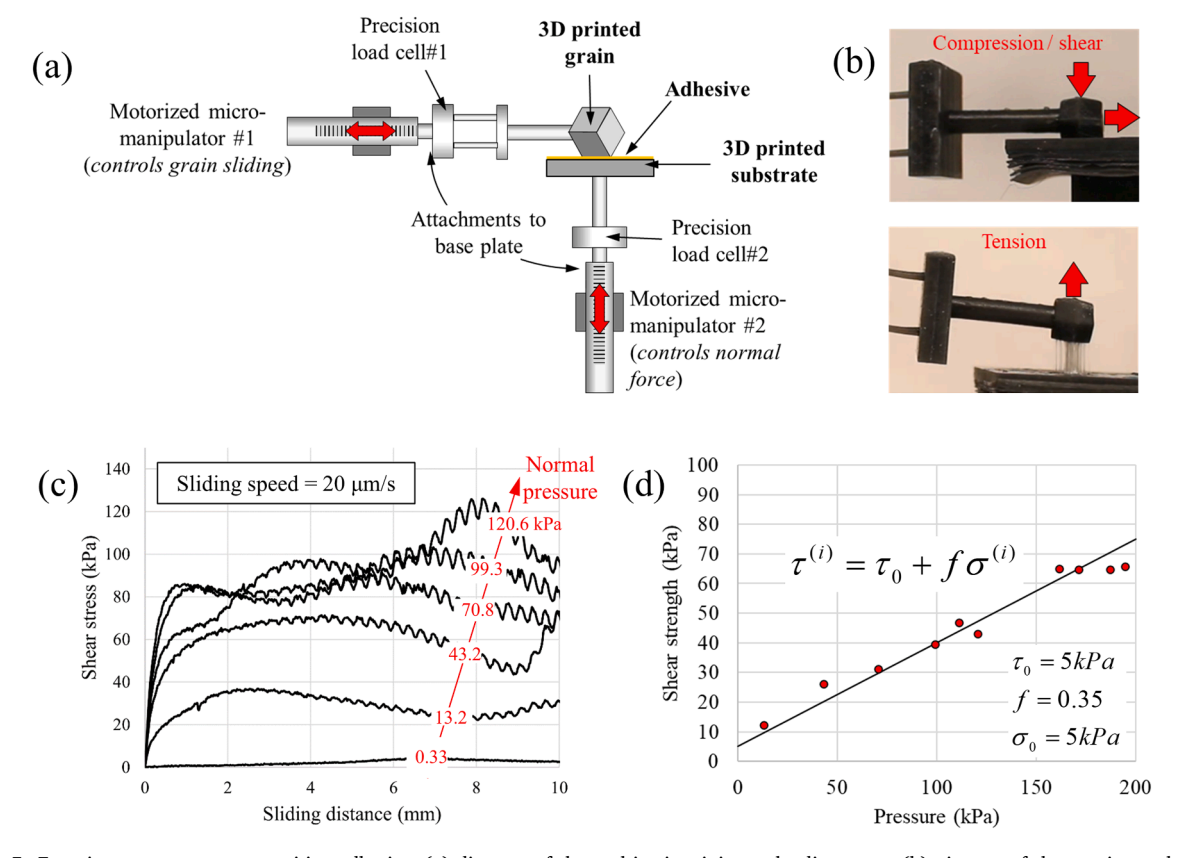


Fig. 5. Experiments on pressure sensitive adhesive. (a) diagram of the multi-axis miniature loading stage; (b) pictures of the test in combined compression / shear, and in tension; (c) shear stress - sliding distance curve for different applied normal pressures; (d) shear strength of the adhesive as function of normal pressure, with the linear approximation used in the model.

crystals is a strong function of the crystal type and loading orientation. Fig. 3 shows the results for those samples that led to a ductile type of response, which was characterized by slip along specific directions within the crystal, while Fig. 4 focuses on samples whose failure was dominated by micro-buckling.

The ductile stress strain curves showed three different stages: (i) linear regime, (ii) progressive softening to peak stress, and (iii) post-peak strain softening. We found no significant differences in strength between the FCC loaded in the $[11\overline{2}]$ direction and the HCP loaded in the $[10\overline{1}0]$ direction. However, their failure modes were quite different: In the FCC crystal a $\{111\}$ slip plane was activated first (Fig. 3b). In the HCP crystal, yielding occurred by activation of prismatic planes ($\{10\overline{1}0\}$). We also performed compression tests on the HCP crystal along the c axis ([0001] loading direction). That direction was much stronger (Fig. 3a) and no clear slip plane was observed. Instead, all grains appeared to slide on one another simultaneously, giving a barreling appearance to the sample from all viewing directions (Fig. 3b). In that loading direction grains from the basal plane were progressively wedged into grains from adjacent basal planes, so that the grains spread apart - referred to as "splaying", which we define as a coordinated grain-sliding mechanism wherein adjacent basal planes wedge apart under c-axis compression, leading to a diffuse expansion of the granular structure in the directions transverse to loading. The absence of available slip planes and this splaying mode of deformation required more stress to activate. While this splaying mechanism is absent at the atomic scale, it commonly occurs in composites, joints, or connections, where external stress or flaws cause layers, fibers, or components to separate (Nguyen et al., 2013; Soldatos, 2018; Yang et al., 2015, 2014).

Fig. 4 compares the compressive response of the FCC crystal when loaded along the $< 1\overline{10} >$ direction, and the HCP when loaded along the $< 11\overline{20} >$ direction. The stress-stain curves (Fig. 4a) showed identical trends: they first increase with a smooth and relatively stiff response up to the peak stress, which was followed by a sharp decrease in stress. In this configuration, the grains formed arrays of parallel columns that carry the compressive force through flat-on-flat contacts, which produced a stiff and strong response. Imaging revealed that grains did not slide or move significantly. Instead, columns of grains buckled collectively near the peak, leading to the rapid softening on the stress–strain curve. In that buckling direction, HCP crystals and FCC had about the same strength, and the crystals were 4 to 16 times stronger in that direction compared to the other directions where inelastic sliding prevailed. Interestingly, after each of the compressive tests the grains could be recovered, recycled, and reassembled into new samples with no loss of overall strength.

5. Granular crystal plasticity models

The experiments presented above suggest that FCC and HCP granular crystals display a broad range of strength and a variety of failure modes. In this section we present models for the various deformation modes of these crystals as a function of loading orien-

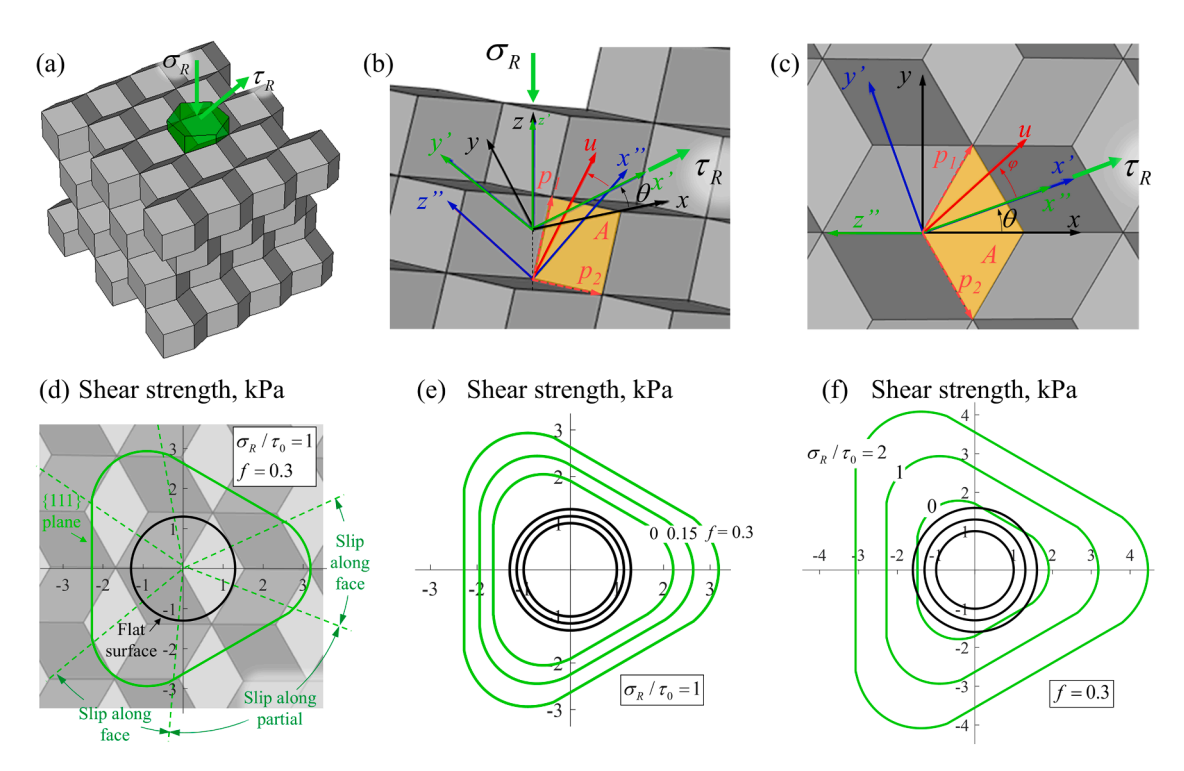


Fig. 6. Modeling the strength of slip planes, with the {111} plane of a FCC crystal as an example. (a) An individual grain (in green) at a resting position on the slip plane and subjected to combinations of normal and shear tractions; Coordinate systems and key directions used in the model in (b) 3D view and (c) top view; (d) Shear strength contour for a flat surface (black circle) and the {111} plane; Effect of (e) friction coefficient and (f) normal applied stress on the shear strength contours.

tation, with the goal to fully capture their mechanics. These models are improved version of the micromechanical models we previously developed for frictional, confined crystals (Karuriya and Barthelat, 2023) and cohesive crystals (Karuriya et al., 2024). Since individual grains interact by contact and through the pressure sensitive adhesive, the first task was to model the mechanical response of the adhesive. The properties of the adhesive were measured using the miniaturized setup show on Fig. 5a (Karuriya et al., 2024). This setup measures the strength of the adhesive in controlled combinations of shear and normal compression (Fig. 5b), as well as in tension. Fig. 5c shows a typical set of shear stress – sliding distance curves, for different amounts of normal compressive forces. Fig. 5d shows the resulting shear strength as function of superimposed normal force. In our previous study, we used a power law to capture this experiment dataset. For the present study, we used a simplified linear approximation, which enabled close-form solutions for the strength of different slip systems:

$$\tau_i = \tau_0 + f\sigma_i \tag{1}$$

The pressure-sensitive adhesive we used also display rate dependencies. To streamline the model, we performed interfaces tests at the same sliding rates as observed in the granular crystal in compression (12 μ m/sec). At the appropriate rates, we identified $\tau_0 \sim 5$ kPa and $f \sim 0.35$ from the experiments. The measured tensile strength of the adhesive was $\sigma_0 \sim 5$ kPa.

Face-on climb: The next level in this model captures the strength of the available slip planes in the granular crystals. To this end we considered the surface a slip plane and its morphology, as well as one grain representative of the adjacent plane of grains in the crystal. Fig. 6 shows an example of this configuration for a {111} plane. The objective in this step was to calculate the shear stress τ_R which must be applied to that grain to dislodge it from its initial position. This shear stress depends on the applied compressive stress σ_R , on the properties of the adhesive, on the morphology of the slip plane and on the in-plane orientation of the applied shear stress with respect to that morphology. The upper grain may be dislodged along a unit vector \overrightarrow{u} , but because of the morphology of the surface the direction \overrightarrow{u} does not, in general, coincide with the direction of applied shear stress. For a face-on climb, the sliding vector \overrightarrow{u} must be contained within a plane region defined by the two edges p_1 and p_2 of the grain face (Fig. 6b). The equilibrium of the upper grain at the onset of failure is written:

$$A_{g}\overrightarrow{t} + \sum_{m}^{c} A_{m}\sigma_{m}\overrightarrow{n}_{c} - \left(\sum_{m}^{c} A_{m}\tau_{m} + \sum_{n}^{t} A_{n}\sigma_{n}\right)\overrightarrow{u} = 0$$

$$(2)$$

Where A_g is the cross-sectional area of the upper grain and \vec{t} is a traction vector applied onto the grain. The second term represents the compressive stresses σ_m transmitted through c grain faces with normal \vec{n}_c . For a face on climb on a {111} plane c=1, but c may be greater for the more complex slip planes described below (all compressive faces, however, always shared the same normal vector \vec{n}_c). The third term represents the resistance to sliding generated by the adhesive, as a force acting directly against the sliding vector \vec{u} . This term includes shear tractions from the grain faces in compression, and tensile tractions from the interfaces which open as the grain is dislodged (t is the number of grain faces which are opening). A_i denotes the individual surface areas of the grain faces involved in sliding and opening. We then use the constitutive equation of the interfaces to write:

$$A_{g}\overrightarrow{t} + \sum_{m}^{c} A_{m}\sigma_{i}\overrightarrow{n}_{c} - \left(\sum_{m}^{c} A_{m}(\tau_{0} + f\sigma_{i}) + \sum_{n}^{t} A_{n}\sigma_{0}\right)\overrightarrow{u} = 0$$
(3)

In most slip plane configurations we considered, there was only one compressive face for a face-on climb, but a few of the most complex slip planes involved more than one face (These compressive faces, however, always shared the same normal vector \vec{n}_c). Finally, the third term represents the resistance of the interfaces: shear resistance from the compressive faces, and tensile traction from the tensile faces. Both of these effects act along the sliding vector \vec{u} . We then write the ratios of surface areas:

$$\begin{cases} \lambda_c = \sum_{m}^{c} A_m / A_g \\ \lambda_t = \sum_{n}^{t} A_n / A_g \end{cases} \tag{4}$$

And rewrite Eq. (3):

$$\vec{t} + \lambda_c \sigma_c \vec{n}_c - (\lambda_c (\tau_0 + f \sigma_c) + \lambda_t \sigma_0) \vec{u} = 0$$
(5)

To project this equation, we considered a coordinate system where x and y are within the slip plane and z is out of plane. The direction x is chosen so that shearing along this direction is aligned with the steepest direction against the contacting face (the angle of steepest climb is denoted ϕ_0). It is useful to consider a second coordinate system (xyz)' where x' is aligned with the direction of shearing (i.e. (xyz) is transformed into (xyz)' by a rotation of θ about the z axis). A third coordinate system (xyz)' is obtained by rotating (xyz)' about the y' axis, so that x'' lies within the plane of the compressive face and z'' coincides with the normal to that face. This rotation is the apparent slope of the climb, which we denote ϕ . This angle can be found with:

$$\tan\phi = \tan\phi_0\cos\theta$$
 (6)

We note again that because of the morphology of the surface the sliding direction \vec{u} does not, in general, coincide with the direction

of applied shear stress. Indeed, in order to satisfy equilibrium sliding generally occurs at a slip angle φ from axis x''. It is now relatively easy to write the components of \overrightarrow{u} and of \overrightarrow{n}_c in the (xyz)'' system. The component of \overrightarrow{t} can also be obtained, but only by transformation matrices from the (xyz) to the (xyz)' to the (xyz)'' coordinate system. Equilibrium is then written:

$$\begin{pmatrix} \tau_R \cos\phi - \sigma_R \sin\phi \\ \sin\phi_0 \sin\theta (\tau_R \sin\phi + \sigma_R \cos\phi) \\ -\tau_R \sin\phi_0 \cos\theta - \sigma_R \cos\phi_0 \end{pmatrix} + \lambda_c \sigma_c \begin{pmatrix} 0 \\ 0 \\ 1 \end{pmatrix} - (\lambda_c \tau_0 + f \lambda_c \sigma_c + \lambda_t \sigma_0) \begin{pmatrix} \cos\varphi \\ \sin\varphi \\ 0 \end{pmatrix} = \begin{pmatrix} 0 \\ 0 \\ 0 \end{pmatrix}$$
 (7)

These three equations can be solved to eliminate σ_c and φ to find the applied shear stress on the slip plane:

$$\tau_R = \frac{-B \pm \sqrt{B^2 - 4AC}}{2A} \tag{8}$$

As a function of:

$$\begin{cases} A = 1 + (\sin\phi_0\sin\theta)^2\tan^2\phi_0\cos^2\theta - (\tan^2\phi_0\cos^2\theta + 1)f^2\sin^2\phi_0\cos^2\theta \\ B = 2\left[\sigma_R\tan\phi_0\cos\theta(\sin^2\phi_0\sin^2\theta - 1) - f\sin\phi_0\cos\theta(\tan^2\phi_0\cos^2\theta + 1)(\lambda_1\tau_0 + \lambda_3\sigma_0 + f\sigma_R\cos\phi_0)\right] \\ C = \sigma_R^2\left(\tan^2\phi_0\cos^2\theta + \sin^2\phi_0\sin^2\theta\right) - (\tan^2\phi_0\cos^2\theta + 1)(\lambda_1\tau_0 + \lambda_3\sigma_0 + f\sigma_R\cos\phi_0)^2 \end{cases} \tag{9}$$

In turn, the slip angle is given by:

$$\sin\varphi = \frac{\sin\phi_0\sin\theta(\tau_R\tan\phi_0\cos\theta + \sigma_R)}{\sqrt{\tan^2\phi_0\cos^2\theta + 1}(\lambda_1\tau_0 + \lambda_3\sigma_0 + f\cos\phi_0(\sigma_R + \tau_R\tan\phi_0\cos\theta))}$$
 (10)

If $\theta=0$ the shear stress is applied along the steepest direction and the slip is zero ($\varphi=0$), as expected. If $\theta\neq 0$, a slip angle develops, and that slip angle increases as θ is increased. At some limit however, equilibrium cannot be sustained, and slip must then occur along one of the edges of the climbing face. Further increasing θ then leads to a configuration where two compressive faces resist the dislodging of the grain. In this case the equilibrium is written:

$$A_{\sigma} \overrightarrow{t} + A_{1}\sigma_{1} \overrightarrow{n}_{1} - A_{1}\tau_{1} \overrightarrow{p} + A_{2}\sigma_{2} \overrightarrow{n}_{2} - A_{2}\tau_{2} \overrightarrow{p} - A_{3}\sigma_{0} \overrightarrow{p} = 0$$

$$\tag{11}$$

In Eq. (11), indices 1 and 2 refer to the areas, stresses and vectors associated with compressive faces 1 and 2. This case, seemingly more complex, is actually easier to solve than the face-on climb because the displacement always occurs along a known partial direction \vec{p} governed by the morphology of the grains on that slip plane. Solving this equation leads to:

$$\tau_R = \frac{\sigma_R + T_f(\lambda_c \tau_0 + \lambda_t \sigma_0)}{C_c \cos\theta + S \sin\theta} \tag{12}$$

with
$$\begin{cases} C_{f} = \frac{sp_{x} - (n_{1y} - n_{2y})fp_{z}}{sp_{z} + (n_{1y} - n_{2y})fp_{x}} \\ S_{f} = \left(\frac{(n_{1x} - n_{2x})p_{z} - (n_{1z} - n_{2z})p_{x}}{sp_{z} + (n_{1y} - n_{2y})fp_{x}}\right) f \\ T_{f} = \frac{s}{sp_{z} + (n_{1y} - n_{2y})fp_{x}} \\ s = \left(\overrightarrow{n}_{2} \times \overrightarrow{n}_{1}\right) . \overrightarrow{p}_{1} \end{cases}$$
(13)

And λ_c , λ_t defined as above in Eq. (4). Fig. 6d shows the results for this model, with the example of the shear strength of a {111} plane in a FCC granular crystal. The triangular shape of the contour of shear strength reflects the triangular symmetry of the morphology of the {111} surface. The easiest sidling directions are along the partials vectors defined as the edges of the contact areas, while the hardest direction are along the steepest climbs on the face of the grains. Depending on the normal applied pressure, the shear strength of the {111} plane is 2 to 5 times higher than the shear strength of the adhesive on a flat surface (shown as back circles on Fig. 6). Fig. 6e and 6f show the shear strength of the slip plane as a function of local friction coefficient and applied normal pressure. As expected, the shear strength increases when these two parameters are increased.

With this model in hand, the strength of the granular crystal in compression can be computed, as a function of loading orientation. For each orientation, the resolved shear stress τ_R and the resolved compressive stress σ_R on each available slip plane i was computed. Since both τ_R and σ_R are proportional to the applied uniaxial stress σ_a , they can be written:

$$\begin{cases} \sigma_{\scriptscriptstyle R}^{(i)} = \alpha^{(i)} \sigma_a \\ \tau_{\scriptscriptstyle R}^{(i)} = \beta^{(i)} \sigma_a \end{cases} \tag{14}$$

where $\alpha^{(i)}$ and $\beta^{(i)}$ are orientation factors computed from the transformation matrices. Replacing the resolved stresses into the failure criterion of the slip planes (Eq. (12) above) produces the applied stress required to activate a slip plane i:

$$\sigma_a^{(i)} = \frac{\sigma_h + T_f(\lambda_c \tau_0 + \lambda_t \sigma_0)}{\beta^{(i)} \left(C_f \cos\theta + S_f \sin\theta \right) - \alpha^{(i)}}$$
(15)

With constants λ_c and λ_t obtained from Eq. (4), constants T_f , C_f and S_f obtained from Eq. (13). The angle θ keeps track of the orientation of the resolved shear traction with respect to the morphology of the slip plane (Fig. 6d). Finally, the yield strength of the crystal along the considered loading direction is the minimum of the computed applied stresses for each of the available slip planes:

$$\sigma_{y} = \min\left(\sigma_{a}^{(i)}\right) \tag{16}$$

This process is repeated over all possible loading orientations for the crystals, producing a full picture of the yield strength of the crystal as function of loading orientation. Fig. 7 shows the results of the model for the FCC crystals when the $\{111\}$ and $\{100\}$ families of slip planes are considered. The first observation is that the strength of the crystal is highly anisotropic, including loading directions where slip is completely forbidden, and the predicted yield strength is infinite. These six loading directions are the on-axis directions in the FCC crystal, where buckling occurs (buckling failure is considered further below in this report). The off-axis directions are also shown, the model predicts a yield strength of 64 kPa along these directions, which agrees well with the experiments (~ 50 kPa). Fig. 7f shows the predicted strength when the $\{100\}$ family of slip planes is considered. This plane is stronger than the $\{111\}$, and as a result the overall strength is also greater than for the $\{111\}$ planes, with a broader range of directions where slip is forbidden. Along the off-axis direction the model predicts a strength of 128 kPa when $\{100\}$ slip is considered, which is two times greater than the strength from the $\{111\}$ planes along the same direction. This observation is consistent with the experiments: $\{111\}$ slip is indeed the prominent failure mechanism of the FCC crystals along the off-axis direction.

We now apply this model to the HCP crystals, considering their five typical slip systems: Basal, prismatic, as well as first order (π 1) second order (π 2) and third order (π 3) pyramidal slip systems. The results are shown in Fig. 8. The basal slip (Fig. 8a) is identical in morphology to the {111} family in FCC. However, in FCC the {111} contains four planes, while in the lower symmetry HCP crystal there is only one basal slip plane. This lack of symmetry is reflected on the yield surface where for a broad range of directions basal slip is not possible, because the loading direction is within the basal plane, or because the loading direction is too close to the c-axis (normal to the basal plane). Fig. 8b—e show the configuration and models used for prismatic and pyramidal planes. The morphologies of these planes are more complex, so that two or more grains must be used as representative elements to capture their strength in the model. As a result of these more complex morphologies, their shear strength is also higher than the basal plane. For the π 2 and π 3 slip systems, there are even forbidden direction of shear within the plane where the grains are interlocked and the predicted shear strength is

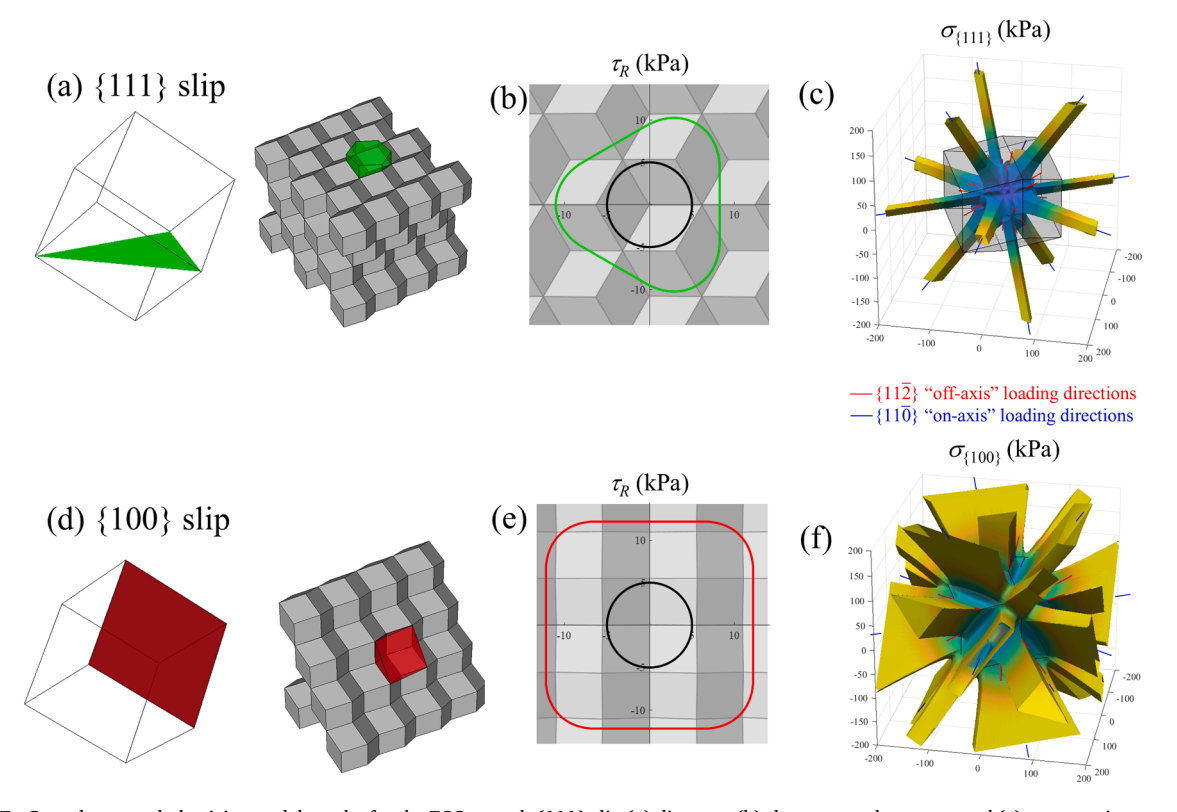


Fig. 7. Granular crystal plasticity model results for the FCC crystal. {111} slip (a) diagram, (b) shear strength contour and (c) compressive strength of the crystal as function of loading orientation. {100} slip (d) diagram, (e) shear strength contour and (f) compressive strength of the crystal as function of loading orientation.

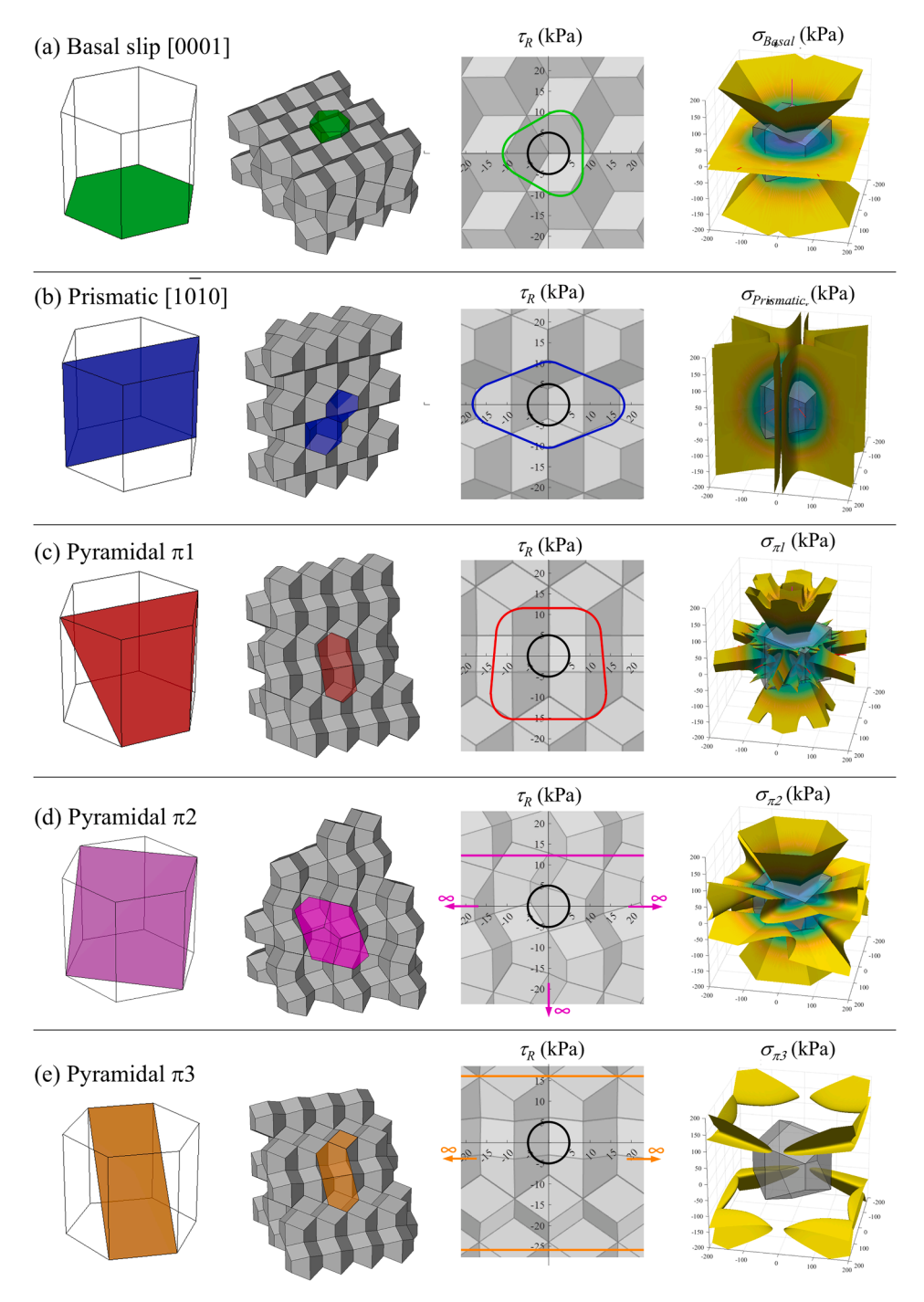


Fig. 8. Granular crystal plasticity model results for the HCP crystal, considering the following slip planes. (a) Basal; (b) prismatic; (c) first order (π 1) pyramidal, (d) second order (π 2) pyramidal and (e) third order (π 3) pyramidal.

infinite. The yield surfaces calculated for each of these slip systems reflect their three-fold symmetries and they appear to be of generally similar strength, except the $\pi 3$ slip system which produces much higher strength with most loading directions completely interlocked geometrically. Some of the compression tests on HCP crystals were performed along the $[10\overline{1}0]$ HCP orientation. The model predicts a compressive strength of 64 kPa along this direction, with failure occurring by prismatic slip. This result is consistent with the experimental observations in terms of failure mode (Fig. 3) and in terms of measured compressive strength (~ 50 kPa). We finally note that none of the five family of slip planes considered on Fig. 8 is activated when loading is applied near the c axis of the HCP crystal. The experiments along that direction (Fig. 3) indeed produced higher compressive strength, with a diffuse type of grain sliding within the

crystal. We captured this failure mode in the next section.

6. Homogeneous grain sliding: a model for splaying failure

Compressive experiments along the c-axis ([0001]) of the HCP crystals reveal an unusual failure mechanism where individual grains simultaneously slide on one another and over large volumes. As opposed to deformation by slip where entire planes of grains move in unison over adjacent planes, in this shorter-range deformation mode each face of every grain either slides or fails in tension. The kinematics of the grains at the local scale, shown on Fig. 9a, can be described as the grains splaying out sideways as they are compressed vertically. For this mechanism to be kinematically acceptable, the compressive load must be applied along or near a long axis of the grains (which connects two opposed corners). Fig. 9b shows two possible splaying directions in the FCC crystal: Splaying within a {111} plane when a compressive stress is applied along a [111] direction and splaying within a {100} plane when a compressive stress is applied along a [100] direction. For each case, the sliding vectors, noted s_1 , s_2 ... are shown. When individual grains participate to slaying failure, they are subjected to two types of tractions: Shear/compression from the applied compressive stresses on the crystals, and tensile tractions at the flanks of the grains, corresponding to the tractions exerted by the adhesive on the opening gaps between the grains. The superposition of these two stress states can be used to predict the applied stress required to trigger splaying failure (Fig. 9c).

In load case 1 (in red on Fig. 9c) a uniaxial pressure σ_a is applied. This compressive stress is transferred to the grain by compressive (σ_{Ra}) and shear (τ_{Ra}) sets of tractions which can be computed from the normal vectors to each of the faces. In load case 2 (in blue on Fig. 9c), tensile tractions σ_0 are imposed on the flanks of the grains, corresponding to the closing tractions exerted by the adhesive on the opening gaps between the grains. These tensile tractions create a lateral tensile stress σ_0 in the mid-section of the bulk of the grain. The grain is maintained in a state of self-equilibrium with compressive (σ_{Rs}) and shear (τ_{Rs}) sets of tractions imposed on the upper and lower sliding faces of the grains, and these tractions create compressive stresses σ_c near the ends of the grain. Since the grain is self-equilibrated, the average stress in the grain subjected to load case 2 must be zero. Therefore, we can compute the compressive stress using:

$$\sigma_c = \frac{V_o}{V_c} \sigma_o \tag{17}$$

Where V_0 is the volume of the mid-section of the grain subjected to σ_0 , and V_c is the volume of the end-sections of the grain subjected to σ_c . The ratio V_0/V_c can be estimated from the geometry of the individual grains and from the direction of splaying. For example, in the FCC crystal splaying along a {111} direction $V_0/V_c \sim 11$. In the FCC crystal splaying along a {100} direction, we estimated $V_0/V_c \sim 5$ from the 3D geometry of the grains. Once σ_c is estimated, the tractions σ_{RS} are computed using the normal

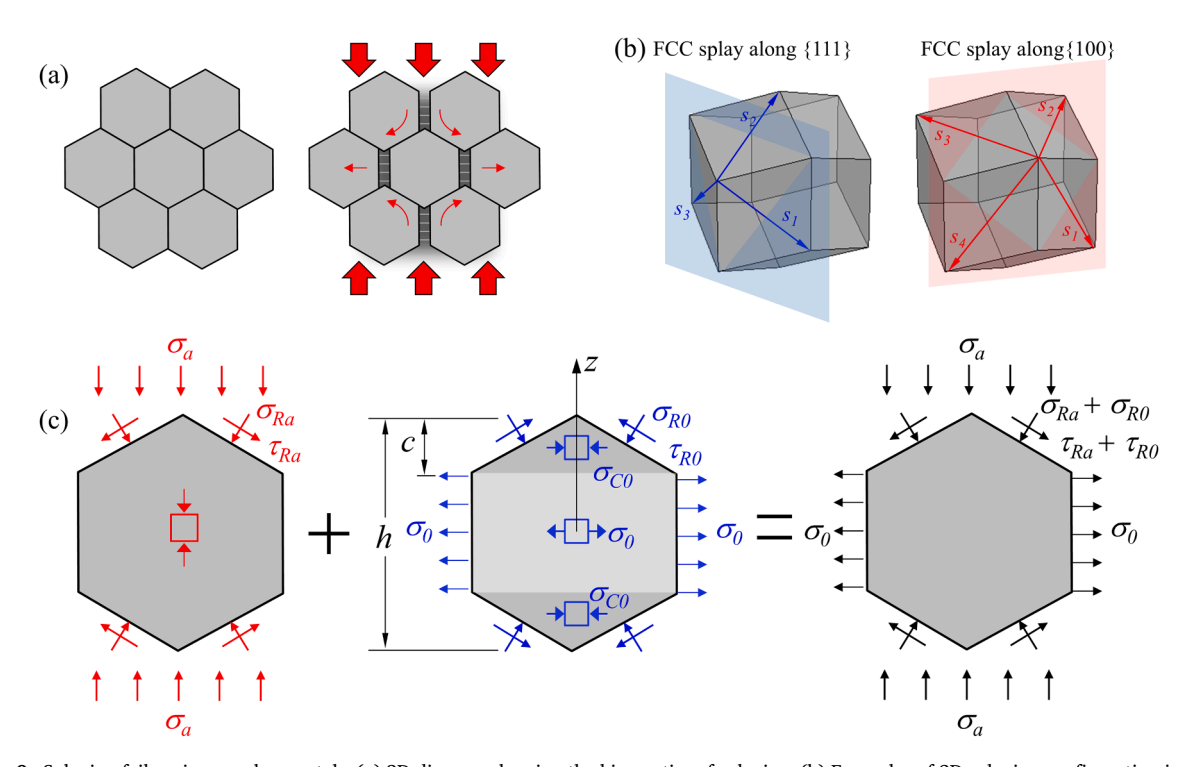


Fig. 9. Splaying failure in granular crystals. (a) 2D diagram showing the kinematics of splaying; (b) Examples of 3D splaying configuration in FCC crystals; (c) the superposition of vertically applied stresses, and tensile stresses applied along the flanks of the grains is used to capture the state of stress in individual grains that undergo splaying failure.

to the sliding faces. Finally, we superimposed stress state 1 and stress state 2 to obtain the stresses corresponding to an individual grain in the splaying structure (Fig. 9c). At the onset of splaying the flanks of the grains fail so σ_0 is the tensile strength of the adhesive. In addition, the sliding faces of the grains also fail, so that failure at these interfaces is written:

$$\tau_{Ra} + \tau_{Rs} = \tau_o + f(\sigma_{Ra} + \sigma_{Rs}) \tag{18}$$

This condition can be used to compute the compressive stress σ_a which must be applied to initiate splaying. This model for splaying was on the three-dimensional geometry of the RD and TRD grains, with the results shown in Fig. 10. As expected, splaying along a {100} direction in FCC is only possible in the direction of loading close to the {100} direction, and splaying along a {111} direction is only possible for loading directions close to $\langle 111 \rangle$. In the FCC crystal the stress required to initiate splaying along {111} with the off-axis loading is 410 kPa, and it is infinite for the $\langle 100 \rangle$ loading direction. For comparison, the compressive stress required to initiate slip along the {111} is 64 kPa (see above), which explains why splaying is not observed in this direction. Splaying in FCC is easier if the crystal is loaded along a [111] or a [100], with predicted compressive strength of 157 kPa and 60 kPa respectively. These predictions will be incorporated into the global failure envelope presented below. Fig. 10c shows the results for the HCP crystal, splaying along the basal plane. Compared to FCC, the lack of symmetries in HCP is evident. Splaying is only possible when the crystal is compressed along directions near the c-axis of the unit cell. The predicted compressive strength for HCP along that direction is 157 kPa, which agrees reasonably well with the experimental strength (200 kPa), considering the assumptions made for the splaying model (perfect structure, simplified stress distribution, and perfect loading alignment).

7. Buckling

The slip-dominated and splaying failures we have considered so far can predict a finite strength for the crystals when loaded in most directions. However, the models also predict sets of specific loading directions where no slip or splaying can be activated. In the experiments, these directions indeed are the strongest direction of the crystals, along which buckling occurs. In the FCC crystal, buckling occurs when compression is along the $< 1\bar{1}0>$ family of directions and in the HCP crystals, buckling occurs along the $< 11\bar{2}0>$ family of directions. In these particular directions, the crystals may be interpreted as columns of grains loaded in parallel, with flaton-flat contact areas perpendicular to the axis of the columns. Importantly, we note that in the experiments the buckling wavelength matches the length of the sample. The implication is that, as opposed to other materials systems such as fiber reinforced composites where buckling strength is a material property (Andrianov et al., 2012), the buckling resistance in our crystals should be interpreted as a structural property, since it probably depends on the length of the sample. To capture buckling and calibrate our buckling model, we first performed compressive tests on individual columns of grains assembled on bonded together with the same adhesive used in the crystals. These individual columns were relatively fragile and delicate to handle, so we limited the height of the columns to eight grains. Fig. 11 shows the resulting compressive force-deflection curves, with associated snapshots. The initial region of the curve was relatively linear, followed by the instability characteristic of buckling. Columns made of Rhombic dodecahedral grains (RD grains that make the FCC crystal) and trapezo-rhombic dodecahedral grains (TRD grains, that make the HCP crystal) grains had about the same initial stiffness, but the buckling strength of TRD grains was slightly higher than the RD grains.

We first used these experiments to calibrate the effective modulus of the grains in compression. The modulus of the resin we used to make the grains is 3 GPa, but the compressive stress is also channeled through a multitude of interfaces, which we expect to be more compliant than the bulk properties of the grain (Johnson, 1985). To estimate the effective compressive modulus of the column E_c , we assumed that the compressive stresses are channeled through an effective cross-section of the column, which we take to be equal to the surface area of a face of the grains. In our experiments this area is A_c =11.5 mm², and it is identical in RD and TRD grains (Fig. 1 above). From the stiffness S of the column in compression, the cross-section A and the length of the column L_c we finally estimate $E_c = SL_c/A_c$ ~100 MPa. As expected, this effective elastic modulus is much lower than the modulus of the grains because of the compliance of the interfaces. The next step was to estimate the critical buckling force of the columns, using Euler's formulae for a clamped-clamp column,

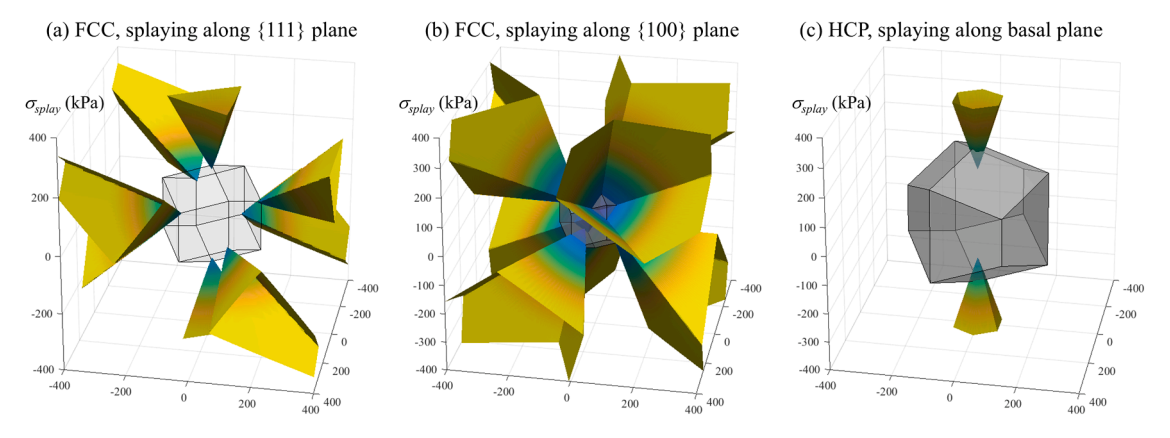


Fig. 10. Results from the splaying model for. (a) FCC crystals along {111} and {100} planes and (b) HCP crystals along the basal plane.

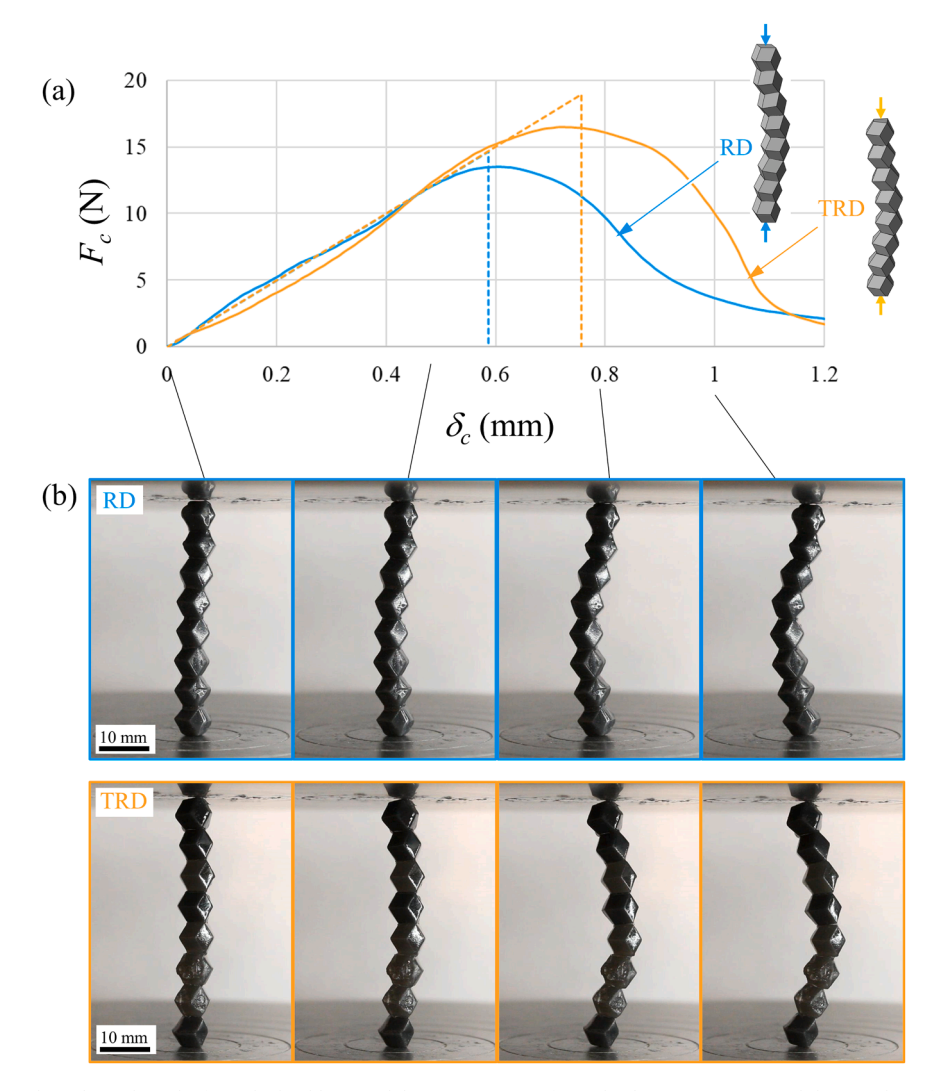


Fig. 11. Experimental results and results from the buckling model (a) compressive force-displacement curves and (b) snapshot of the samples during the test.

assuming that the rotation of the end grains is prevented by the loading platforms:

$$F_{cr} = 4\pi^2 \frac{E_c I_{\min}}{L_c^2} \tag{19}$$

Where I_{\min} is the minimum second moment of area for the cross section. For RD $I_{\min} \sim 7.8$ mm⁴ and for TRD $I_{\min} \sim 10.1$ mm⁴. Fig. 11a shows the model with the stiffness fit to the initial part of the curve, and the buckling force. The model captures the buckling force well, and it properly predicts that the TRD column is slightly stronger than the RD column. We now consider the granular crystal along the buckling direction as an ensemble of N=25 columns of grains in parallel. The critical buckling stress is written:

$$\sigma_{cr} = 4\pi^2 N \frac{E_c I_{\min}}{A_c L^2} \tag{20}$$

Where L is the length of the crystal. This model gives an estimate of $\sigma_{cr} \sim 0.1$ MPa for FCC and HCP crystals, which is only about 1/10 of the experimental buckling strength measured on the granular crystal. This value should however be considered as a lower bound, since the model so far ignored the interaction between individual columns of grains in the crystal. An upper bound can be gained for the buckling strength by assuming that grains from adjacent columns are perfectly bonded. In this case, the crystal buckles as a homogenous solid and the buckling strength is written:

$$\sigma_{cr} = 4\pi^2 \frac{E_c I}{A L^2} \tag{21}$$

This upper bound model predicts $\sigma_{cr} \sim 10$ MPa for FCC and HCP crystals, which is about 10 times the experimental buckling strength measured on the granular crystal. More refined estimates for the buckling stress for the crystal would require capturing the interactions between the columns through direct contact and adhesion, which was beyond the scope of this study.

8. Comparison of FCC and HCP strength and failure modes

By combining all possible failure modes (granular plasticity along slip planes, splaying and buckling), we finally generated the 3D failure envelopes for FCC and HCP crystals under arbitrary loading directions and considering all failure modes, shown in Fig. 12. In these plots, the compressive strength of the crystal was normalized by the strength of the interface τ_0 . These envelopes confirm the strong anisotropy in the strength of both crystals, and the various failure modes that can be achieved along specific crystals and specific direction. The FCC crystal shows a six-fold symmetry due to the regular polyhedral shape of its grains. On most of the loading directions for the FCC, a {111} slip plane is activated, which can also be seen in radial pie charts that consider all loading directions and

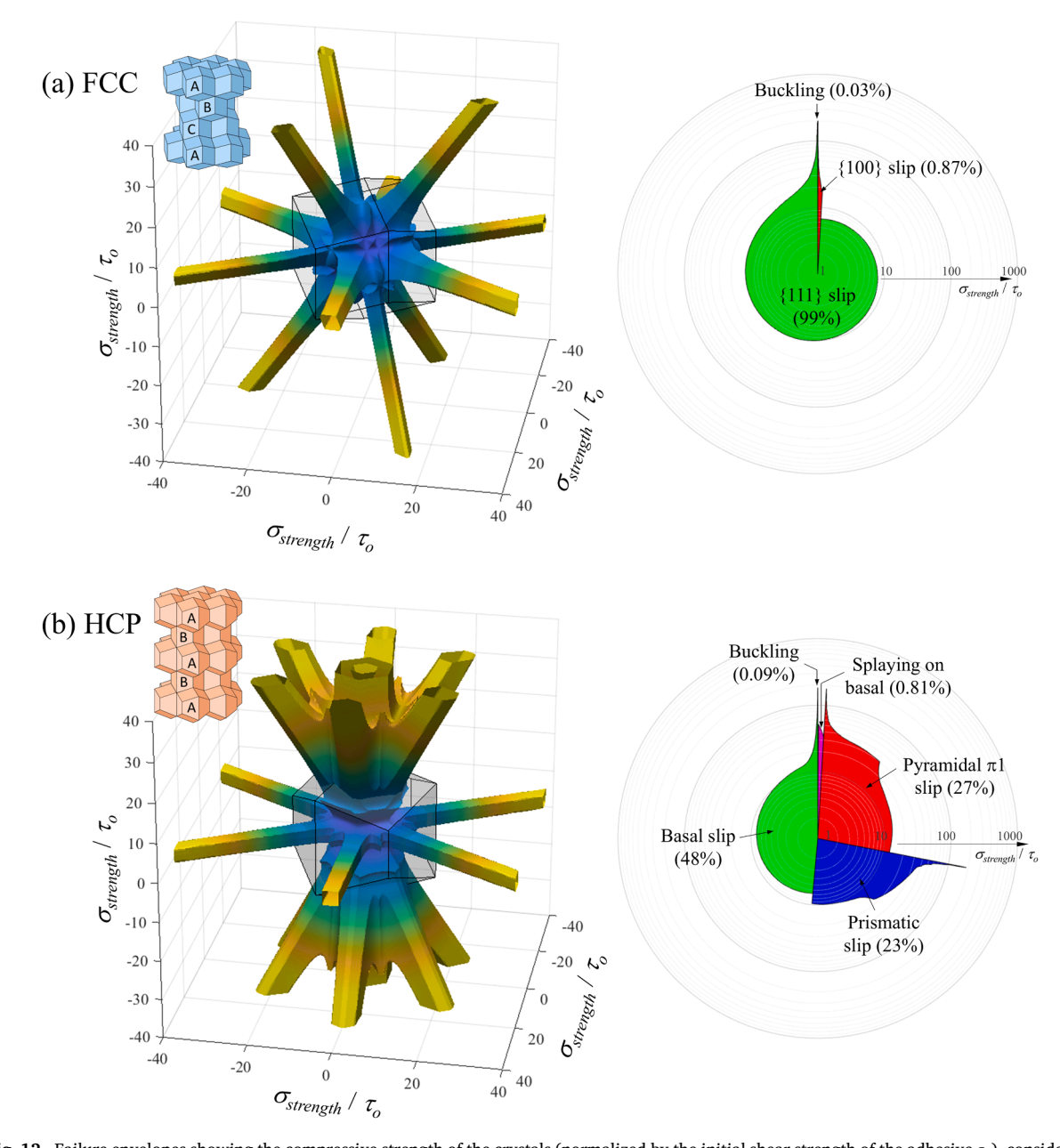


Fig. 12. Failure envelopes showing the compressive strength of the crystals (normalized by the initial shear strength of the adhesive τ_0), considering all failure modes and radial pie chart showing the prominence and strength of each failure mode for (a) FCC crystals and (b) HCP crystals.

the relative prominence of each failure mode (Fig. 12a). {111} slip plane occurs in 99% of the loading directions in FCC. {100} slip planes and buckling are activated along less than 1% of the loading directions (Fig. 12a). Fig. 12b shows the results for the HCP crystal. We first note that the response of the crystal, when loading within the basal plane, is remarkably similar to the FCC crystal loading within the {111} plane (both are the horizontal planes on Fig. 12a, b). However, as the loading direction deviates from that plane, HCP shows significant differences with FCC, mainly because some of the symmetries are broken with the geometrical transition from RD to TRD grains, and from FCC to HCP. This results in more varieties in failure modes, with basal slip (48% of the loading direction), prismatic slip (23%) and pyramidal π 1 (27%) being the most prominent. Buckling and splaying also occur, but only along specific loading directions (and for less than 2% of loading directions). While there are more types of slips that can be activated in HCP compared to FCC, prismatic and pyramidal π 1 require more compressive stress than the basal slip plane and the FCC {111} plane to activate. As a result, the strength of the HCP crystal, averaged over all possible loading directions, is σ 0 > σ 16, which is 45% greater than the average strength in the FCC crystal (σ 11).

9. Summary

Randomly distributed granular materials offer a rich landscape of mechanisms but their tunability is limited. In this report we further explored fully dense granular crystals as a way to tune inelastic deformation mechanisms and strength at the millimeter scales and in three dimensions. Combining principles from crystallography and granular mechanics, we fabricated and tested cohesive HCP granular crystals and compared them with the FCC crystals we previously characterized (Karuriya et al., 2024; Karuriya and Barthelat, 2024, 2023). We also presented a new streamlined version of our previously developed granular plasticity model (Karuriya et al., 2024), which agreed well with the experimental results on FCC and HCP crystals, and which we used to compare deformation mechanisms. An additional model to capture splaying also agreed well with experiments on HCP, and relatively simple models for buckling provided lower and upper bounds that agreed with the experiments for this particular failure mode. Geometrically, switching from an FCC to a HCP architecture is remarkably simple and only involves a 60° rotation about the midplane of individual dodecahedral grains. However, this rotation has profound effects on the mechanics and strength of the crystals. First, the grains assemble into the ABABA sequence for HCP instead of the ABCABC sequence of FCC. Several symmetries are also broken in this geometrical transformation, and while additional slip systems are made available (prismatic, pyramidal...) compared to the {111} family in FCC, each of the families in HCP contain a smaller number of total slip planes. As a result, slip in HCP is in general more difficult to activate resulting in an average strength 50% greater than in FCC, a trend which is reminiscent of HCP and FCC metals (Jiang et al., 2023; Niu et al., 2018; Yang et al., 2018), Granular HCP and FCC crystals indeed share many of the characteristics and trends from their atomic-scale counterpart from metallurgy. In both systems, large deformations are mediated by slip along specific crystallographic planes, which are easy to observe in our granular crystals as well as in metals, especially in nanopillars under compression (Greer and Nix, 2006; Uchic et al., 2004). There are, however, major differences between these two systems. Metallic bonds in plasticity are non-directional, while in our granular crystals the adhesive-mediated grain contact and sliding is highly directional. This fundamental difference becomes particularly evident when examining HCP structures: while deformation twinning is prominent in HCP metals (Arul Kumar et al., 2016; Meyers et al., 2001) we did not observe any twinning in our granular HCP crystals, probably because the angular features of the grains hinder their rotation. Other mechanisms we observed are not present in metals: micro-buckling in FCC and HCP, and splaying in HCP crystals loaded along the c-axis.

Interestingly, traditional plasticity and granular plasticity both show size effects, but not for the same reasons. In nanopillars, strength increases monotonically with decreasing diameter due to dislocation starvation effects below ~ 100 nm (Greer and Nix, 2006; Uchic et al., 2004). Granular crystals also display size effect, but for other reasons: Smaller granular crystals are more confined, which frustrates the full formation of slip planes and which increase strength (Karuriya and Barthelat, 2024). This departure of crystallographic symmetries from traditional defect physics enables new architectural control strategies, offering powerful and versatile platforms for new generation mechanical metamaterials with tunable inelastic deformation, energy absorption and strength. The addition of soft adhesives at the interfaces provides additional opportunities to tune the mechanical response. In particular, the granular architecture amplifies the properties of the adhesive by about one order of magnitude, so that attractive rheologies maybe be translated into useful responses in compression. To increase strength further, numerous extensions are possible including tuning the aspect ratio of the FCC or HCP cells as described in classical plasticity, using defects such as vacancies, dislocations or irregularities as strengthening agents, or manipulate structural and property gradients. While these mechanical responses are finely tuned and the performance of these granular crystals is improved, one should also make sure that recyclability, one of their most attractive features, is preserved: Individual grains can be disassembled, cleaned and reused into new structures without loss of strength.

CRediT authorship contribution statement

Tian Gao: Writing – review & editing, Writing – original draft, Visualization, Validation, Methodology, Investigation, Formal analysis, Data curation. **Ashta Navdeep Karuriya:** Writing – review & editing, Writing – original draft, Visualization, Validation, Methodology, Investigation, Formal analysis, Data curation. **Francois Barthelat:** Writing – review & editing, Writing – original draft, Visualization, Validation, Supervision, Software, Resources, Project administration, Methodology, Investigation, Funding acquisition, Formal analysis, Data curation, Conceptualization.

Declaration of competing interest

The authors declare that they have no known competing financial interests or personal relationships that could have appeared to influence the work reported in this paper.

Acknowledgments

This work was supported by the US National Science Foundation (Mechanics and Materials and Structures, Award CMMI-2033991) and by the Army Research Office under Grant Number W911NF-24-2-0126. The views and conclusions contained in this document are those of the authors and should not be interpreted as representing the official policies, either expressed or implied, of ARO or the U.S. Government. The U.S. Government is authorized to reproduce and distribute reprints for Government purposes notwithstanding any copyright notation herein.

Supplementary materials

Supplementary material associated with this article can be found, in the online version, at doi:10.1016/j.jmps.2025.106305.

Data availability

All data are available in the main text or the supplementary information.

References

Aleene's Repositionable Tacky Spray 10 oz. [WWW Document], 2025 . Aleene's Prem. Glue. URL https://www.aleenes.com/aleenes-repositionable-tacky-spray (accessed 7.21.23).

AlMahri, S., Grega, I., Shaikeea, A.J.D., Wadley, H.N.G., Deshpande, V.S., 2023. Underexcitation prevents crystallization of granular assemblies subjected to high-frequency vibration. Proc. Natl. Acad. Sci. 120, e2306209120. https://doi.org/10.1073/pnas.2306209120.

Andrianov, I.V., Kalamkarov, A.L., Weichert, D., 2012. Buckling of fibers in fiber-reinforced composites. Compos. Part B Eng. 43, 2058–2062. https://doi.org/10.1016/j.compositesb.2012.01.055.

Antonangeli, D., Merkel, S., Farber, D.L., 2006. Elastic anisotropy in hcp metals at high pressure and the sound wave anisotropy of the Earth's inner core. Geophys. Res. Lett. 33. https://doi.org/10.1029/2006GL028237.

Arul Kumar, M., Beyerlein, I.J., McCabe, R.J., Tomé, C.N., 2016. Grain neighbour effects on twin transmission in hexagonal close-packed materials. Nat. Commun. 7, 13826. https://doi.org/10.1038/ncomms13826.

Athanassiadis, A.G., Miskin, M.Z., Kaplan, P., Rodenberg, N., Lee, S.H., Merritt, J., Brown, E., Amend, J., Lipson, H., Jaeger, H.M., 2014. Particle shape effects on the stress response of granular packings. Soft Matter 10, 48–59. https://doi.org/10.1039/C3SM52047A.

Barthelat, F., Yin, Z., Buehler, M.J., 2016. Structure and mechanics of interfaces in biological materials. Nat. Rev. Mater. 1, 1–16. https://doi.org/10.1038/natrevmats.2016.7.

Behringer, R.P., Bi, D., Chakraborty, B., Clark, A., Dijksman, J., Ren, J., Zhang, J., 2014. Statistical properties of granular materials near jamming. J. Stat. Mech. Theory Exp. 2014, P06004. https://doi.org/10.1088/1742-5468/2014/06/P06004.

Behringer, R.P., Chakraborty, B., 2018. The physics of jamming for granular materials: a review. Rep. Prog. Phys. 82, 012601. https://doi.org/10.1088/1361-6633/aadc3c.

Damasceno, P.F., Engel, M., Glotzer, S.C., 2012. Predictive self-assembly of polyhedra into complex structures. Science 337, 453–457. https://doi.org/10.1126/science.1220869.

de Gennes, P.G., 1998. Reflections on the mechanics of granular matter. Phys. Stat. Mech. Appl. 261, 267–293. https://doi.org/10.1016/S0378-4371(98)00438-5. Greer, J.R., Nix, W.D., 2006. Nanoscale gold pillars strengthened through dislocation starvation. Phys. Rev. B 73, 245410. https://doi.org/10.1103/PhysRevB.73.245410.

Henzie, J., Grünwald, M., Widmer-Cooper, A., Geissler, P.L., Yang, P., 2012. Self-assembly of uniform polyhedral silver nanocrystals into densest packings and exotic superlattices. Nat. Mater. 11, 131–137. https://doi.org/10.1038/nmat3178.

Jaeger, H.M., Nagel, S.R., Behringer, R.P., 1996. Granular solids, liquids, and gases. Rev. Mod. Phys. 68, 1259–1273. https://doi.org/10.1103/RevModPhys.68.1259. Jiang, Q., Chen, Y., Shuai, Q., Liu, F., Li, L., He, C., Zhang, H., Wang, C., Liu, Y., Wang, Q., 2023. Fatigue-induced HCP-to-FCC phase transformation resulting in two FCC-Zr variants in pure zirconium. Materials 16, 6215. https://doi.org/10.3390/ma16186215.

Johnson, K.L., 1985. Contact Mechanics. Cambridge University Press, Cambridge. https://doi.org/10.1017/CBO9781139171731.

Callister Jr, W.D., Rethwisch, D.G., 2020. Materials Science and Engineering: An Introduction. John Wiley & Sons.

Karuriya, A.N., Barthelat, F., 2024. Plastic deformations and strain hardening in fully dense granular crystals. J. Mech. Phys. Solids 186, 105597. https://doi.org/10.1016/j.jmps.2024.105597.

Karuriya, A.N., Barthelat, F., 2023. Granular crystals as strong and fully dense architectured materials. Proc. Natl. Acad. Sci. 120, e2215508120. https://doi.org/10.1073/pnas.2215508120.

Karuriya, A.N., Simoes, J., Barthelat, F., 2024. Fully dense and cohesive FCC granular crystals. Extrem. Mech. Lett. 71, 102208. https://doi.org/10.1016/j.eml.2024.102208.

Kettle, S.F.A., Norrby, L.J., 1994. The Wigner-Seitz unit cell. J. Chem. Educ. 71, 1003. https://doi.org/10.1021/ed071p1003.

Lin, Q., Liu, J., An, X., Wang, H., Zhang, Y., Liao, X., 2018. Cryogenic-deformation-induced phase transformation in an FeCoCrNi high-entropy alloy. Mater. Res. Lett. 6, 236–243. https://doi.org/10.1080/21663831.2018.1434250.

Lu, S., Sun, X., Tian, Y., An, X., Li, W., Chen, Y., Zhang, H., Vitos, L., 2023. Theory of transformation-mediated twinning. PNAS Nexus 2. https://doi.org/10.1093/pnasnexus/pgac282 pgac282.

Maire, E., Redston, E., Persson Gulda, M., Weitz, D.A., Spaepen, F., 2016. Imaging grain boundary grooves in hard-sphere colloidal bicrystals. Phys. Rev. E 94, 042604. https://doi.org/10.1103/PhysRevE.94.042604.

Meyers, M.A., Vöhringer, O., Lubarda, V.A., 2001. The onset of twinning in metals: a constitutive description. Acta Mater. 49, 4025–4039. https://doi.org/10.1016/S1359-6454(01)00300-7.

- Mirkhalaf, M., Zhou, T., Barthelat, F., 2018. Simultaneous improvements of strength and toughness in topologically interlocked ceramics. Proc. Natl. Acad. Sci. 115, 9128–9133. https://doi.org/10.1073/pnas.1807272115.
- Nguyen, T.D., Mao, S., Yeh, Y.W., Purohit, P.K., McAlpine, M.C., 2013. Nanoscale flexoelectricity. Adv. Mater. 25, 946–974. https://doi.org/10.1002/adma/201203852
- Niu, C., LaRosa, C.R., Miao, J., Mills, M.J., Ghazisaeidi, M., 2018. Magnetically-driven phase transformation strengthening in high entropy alloys. Nat. Commun. 9, 1363. https://doi.org/10.1038/s41467-018-03846-0.
- Onoda, G.Y., Liniger, E.G., 1990. Random loose packings of uniform spheres and the dilatancy onset. Phys. Rev. Lett. 64, 2727–2730. https://doi.org/10.1103/ PhysRevLett.64.2727.
- Radjai, F., Roux, J.N., Daouadji, A., 2017. Modeling granular materials: century-long research across scales. J. Eng. Mech. 143, 04017002. https://doi.org/10.1061/(ASCE)EM.1943-7889.0001196.
- Schall, P., Cohen, I., Weitz, D.A., Spaepen, F., 2004. Visualization of dislocation dynamics in colloidal crystals. Science 305, 1944–1948. https://doi.org/10.1126/science.1102186.
- Soldatos, K.P., 2018. On the characterisation of polar fibrous composites when fibres resist bending–Part II: connection with anisotropic polar linear elasticity. Int. J. Solids Struct. 152–153, 1–11. https://doi.org/10.1016/j.ijsolstr.2018.08.022.
- Uchic, M.D., Dimiduk, D.M., Florando, J.N., Nix, W.D., 2004. Sample dimensions influence strength and crystal plasticity. Science 305, 986–989. https://doi.org/10.1126/science.1098993.
- Villarruel, F.X., Lauderdale, B.E., Mueth, D.M., Jaeger, H.M., 2000. Compaction of rods: relaxation and ordering in vibrated, anisotropic granular material. Phys. Rev. E 61, 6914–6921. https://doi.org/10.1103/PhysRevE.61.6914.
- Yang, J., Han, C.R., Zhang, X.M., Xu, F., Sun, R.C., 2014. Cellulose nanocrystals mechanical reinforcement in composite hydrogels with multiple cross-links: correlations between dissipation properties and deformation mechanisms. Macromolecules 47, 4077–4086. https://doi.org/10.1021/ma500729q.
- Yang, J., Zhang, X.M., Xu, F., 2015. Design of cellulose nanocrystals template-assisted composite hydrogels: insights from static to dynamic alignment. Macromolecules 48, 1231–1239. https://doi.org/10.1021/ma5026175.
- Yang, J.X., Zhao, H.L., Gong, H.R., Song, M., Ren, Q.Q., 2018. Proposed mechanism of HCP → FCC phase transition in titianium through first principles calculation and experiments. Sci. Rep. 8, 1992. https://doi.org/10.1038/s41598-018-20257-9.